

RADIATION FROM AN ECCENTRIC COATED CYLINDER WITH SLOTS OF ARBITRARY SIZES AND POSITIONS

M. A. Mushref

P. O. Box 9772, Jeddah 21423, Saudi Arabia

Abstract—The transverse electric (TE) field patterns and characteristics are considered for a cylinder with N infinite axial slots of arbitrary opening size and position. The cylinder is a thin circular conductor and covered by an eccentric material. Radiations are determined by applying the boundary conditions to the cylindrical wave functions of the fields. The addition theorem of Bessel functions is employed to find an infinite-series solution in Fourier-Bessel series form. Results are achieved by reducing the produced infinite series to a finite number of terms and judged against other published data. Numerical and graphical results for different values are also presented and discussed for small eccentricities.

1. INTRODUCTION

The study of field characteristics from slotted cylindrical antennas is an essential problem in electromagnetic field theory and has been the subject of several former researches [1–4]. There is an ongoing requirement to improve and develop radiating systems for applications in aircrafts and missiles that will not weaken or change the aerodynamic properties of the vehicle. In addition, slotted cylinders in particular structures achieved various commercial applications in frequency modulation (FM) and television (TV) transmission and reception. The horizontal polarization of the slot-in-cylinder used for FM and TV broadcasting possesses significant advantages over the ordinary dipole antenna [5]. Besides, lightweight, simplicity of assembly and high radiated power made this type of antennas suitable for other applications such as radars, satellite communications and global positioning systems (GPS) [6].

In 1950, Silver and Saunders derived expressions for the external field produced by a slot of arbitrary shape. The far field was obtained

by applying the method of steepest descent to the Fourier integrals in the solution [1]. The results obtained were also applied by Bailin in 1955 to the cases of narrow-width half-wavelength slots in infinite cylinders with large radii [2]. In 1956, Hurd derived the radiation patterns of an axial slot in a dielectric coated circular cylinder and made some comparisons with experimental results [3]. Additionally, Wait and Mientka, in 1957, presented the fields produced by an arbitrary slot on a circular cylinder with a cocentric dielectric coating. The far zone expressions were developed using a saddle-point method applied to the derived integrals [4].

However, earlier investigations did not consider possible effects to radiations of N arbitrary placed axial slots with different opening sizes and when the conducting cylinder and the coating material are both eccentric. This proposed construction can highly improve radiation directivity and other field characteristics that can be easily adapted with sizes and positions of the axial slots.

2. ANTENNA STRUCTURE

Problems with cylindrical boundaries and surfaces are usually better solved in cylindrical coordinates. The problem stated in this paper is solved in the two dimensional circular cylindrical coordinate system

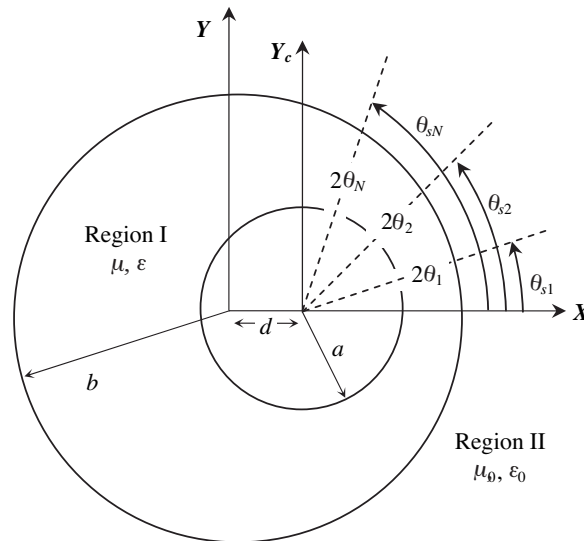


Figure 1. Geometry of the problem.

with orientation (r, ϕ) . As shown in Figure 1, the global coordinate system (r, ϕ) is defined at the center of the dielectric coating material and the local coordinate system (r_c, ϕ_c) is defined at the center of the slotted metallic cylinder. The center of the local coordinate system is positioned at $x = d$ with respect to the global coordinate system.

Here, the transverse electric (TE) field is to be found for N infinite axial slots in a circular metallic cylinder coated with a dielectric material as illustrated in Figure 1. The cylinder is assumed to be a thin perfect electric conductor with radius a and with infinite extent along the z -axis. On the cylinder surface N slots are axially opened with angular apertures of $2\theta_1, 2\theta_2, 2\theta_3, \dots, 2\theta_N$ located at $\theta_{s1}, \theta_{s2}, \theta_{s3}, \dots, \theta_{sN}$ respectively with respect to the x -axis. The cylinder is totally coated by an eccentric layer with radius b and assumed to be homogenous, linear and isotropic and characterized by permittivity ε and permeability μ . The region out of the coating material for all $r > b$ and $0 \leq \phi \leq 2\pi$ is assumed to be free space with ε_0 and μ_0 . As shown in Figure 1, the dielectric material and free space are considered as region I and region II respectively.

3. MATHEMATICAL FORMULATION

The Helmholtz scalar wave equation is first solved in the circular cylindrical coordinate system in r and ϕ . Going after the separation of variables technique, the solution is a Bessel or Hankel function in r multiplied by a complex exponential in ϕ . The structure shown in Figure 1 implies the magnetic field to be represented by a Fourier-Bessel exponential series. In region I this is represented by a summation of a harmonic function multiplied by Bessel functions as [3]:

$$H_z^I = \sum_{n=-\infty}^{\infty} e^{in\phi} \{\alpha_n J_n(kr) + \beta_n Y_n(kr)\} A_n \quad (1)$$

In region II the magnetic field radiates from the structure and therefore the Hankel function is assumed and multiplied by a harmonic function as [3]:

$$H_z^{II} = \sum_{n=-\infty}^{\infty} e^{in\phi} H_n^{(2)}(k_0 r) A_n \quad (2)$$

where α_n, β_n and A_n are unknown coefficients and $i = \sqrt{-1}$. k and k_0 are the dielectric coating and free space wave numbers respectively given by $k = 2\pi/\lambda$ and λ is the wavelength. $J_n(x)$ and $Y_n(x)$ are Bessel functions of the first and the second type respectively with order n and

argument x . $H_n^{(2)}(x)$ is the outgoing Hankel function of the second type with order n and argument x .

4. ANALYTICAL SOLUTION

We can apply the boundary conditions to find α_n , β_n and A_n coefficients. According to the geometry of the structure shown in Figure 1 the boundary conditions with respect to the global coordinate are continuity of both tangential electric E_ϕ and magnetic H_z fields for all ϕ at $r = b$, that is:

$$H_z^I = H_z^{II} \quad \text{for } r = b \text{ and } 0 \leq \phi \leq 2\pi \quad (3)$$

$$E_\phi^I = E_\phi^{II} \quad \text{for } r = b \text{ and } 0 \leq \phi \leq 2\pi \quad (4)$$

where E_ϕ is derived from Maxwell's equations as $E_\phi = (i/\omega\epsilon)(\partial H_z/\partial r)$ [3].

Equations (3) and (4) are solved by employing the orthogonality of the complex exponential functions. Each side is multiplied by $e^{-iq\phi}$ and integrated over ϕ from 0 to 2π where q is an integer. We respectively get:

$$\alpha_n J_n(kb) + \beta_n Y_n(kb) = H_n^{(2)}(k_0b) \quad (5)$$

$$\alpha_n J'_n(kb) + \beta_n Y'_n(kb) = e_r H_n^{(2)'}(k_0b) \quad (6)$$

where $e_r = \sqrt{\epsilon_r/\mu_r}$ and the prime notation designates differentiation with respect to the argument.

Solving Equations (5) and (6) by elimination for α_n and β_n we respectively obtain:

$$\alpha_n = \frac{\pi kb}{2} \left[H_n^{(2)}(k_0b) Y'_n(kb) - e_r H_n^{(2)'}(k_0b) Y_n(kb) \right] \quad (7)$$

$$\beta_n = \frac{-\pi kb}{2} \left[H_n^{(2)}(k_0b) J'_n(kb) - e_r H_n^{(2)'}(k_0b) J_n(kb) \right] \quad (8)$$

The third boundary condition is expressed in the local coordinate system. At $r_c = a$ the tangential electric field vanishes in region I for all values of ϕ_c except at the slots where it has a constant value of E_{oL} [7, 8]. That is:

$$E_\phi^I = E_{oL} \quad \text{for } r_c = a \text{ and } |\phi_c - \theta_{sL}| < \theta_L \quad L = 1, \dots, N \quad (9)$$

The addition theorem of Bessel functions should be used in this case. From [9, 10] we have:

$$T_m(kr)e^{im\phi} = \sum_{p=-\infty}^{\infty} (-1)^p \begin{cases} T_{m+p}(kr_c) J_p(kd) e^{i(m+p)\phi_c} & r_c > d \\ T_{m+p}(kd) J_p(kr_c) e^{-ip\phi_c} & r_c < d \end{cases} \quad (10)$$

where $T_m(x)$ can be $J_m(x)$ or $Y_m(x)$ and m and p are integers.

By applying Equation (10) to Equation (9) we can simplify the outcome to be:

$$\begin{aligned} & \sum_{n=-\infty}^{\infty} A_n (-1)^{m-n} \left\{ \alpha_n \begin{matrix} J'_m(ka) \\ J'_{m-n}(kd) \end{matrix} + \beta_n \begin{matrix} Y'_m(ka) \\ Y'_{m-n}(kd) \end{matrix} \right\} \begin{matrix} J_{m-n}(kd) & a > d \\ J_m(ka) & a < d \end{matrix} \\ &= \frac{\omega \varepsilon}{ikm\pi} \sum_{L=1}^N E_{oL} \sin(m\theta_L) e^{-im\theta_{sL}} \end{aligned} \quad (11)$$

For very small values of θ_L , Equation (11) can be simplified to:

$$\begin{aligned} & \sum_{n=-\infty}^{\infty} A_n (-1)^{m-n} \left\{ \alpha_n \begin{matrix} J'_m(ka) \\ J'_{m-n}(kd) \end{matrix} + \beta_n \begin{matrix} Y'_m(ka) \\ Y'_{m-n}(kd) \end{matrix} \right\} \begin{matrix} J_{m-n}(kd) & a > d \\ J_m(ka) & a < d \end{matrix} \\ &= \frac{\omega \varepsilon}{ik\pi} \sum_{L=1}^N E_{oL} \theta_L e^{-im\theta_{sL}} \end{aligned} \quad (12)$$

The special case of $N = 2$, $E_{o1} = E_{o2} = E_0$, $2\theta_1 = 2\theta_2 = \theta_0$, $\theta_{s1} = 0$ and $\theta_{s2} = \pi$ implies the right side of Equation (12) to be $\frac{E_0 \omega \varepsilon \theta_0}{2ik\pi} [1 + \cos(m\pi)]$ as in [7, 8].

For small values of d the summation rapidly converges and thus Equation (2) can be further simplified if expressed in matrix form and therefore we can find the coefficients A_n as:

$$[A_n]_{n \times 1} = [Z_{n,m}]_{n \times m}^{-1} [f_m]_{m \times 1} \quad (13)$$

where $Z_{n,m}$ is the second factor in the left side of Equation (12) and f_m is the right side of the same equation. The matrix $[Z_{n,m}]_{m \times n}$ in Equation (13) is a non-singular square matrix.

5. RADIATION CHARACTERISTICS

The asymptotic expression of the Hankel function can be used for Equation (2) and thus the radiated field can be evaluated at a far point as [11, 12]:

$$H_z^{\text{II}} = e^{-i(k_0 r - \pi/4)} P(\phi) \sqrt{\frac{2}{\pi k_0 r}} \quad (14)$$

where $P(\phi)$ is the far radiated field pattern given by:

$$P(\phi) = \sum_{n=-\infty}^{\infty} i^n A_n e^{in\phi} \quad (15)$$

The antenna gain and the aperture conductance per unit length λ_0 are major quantities in the study of the antenna characteristics. By Equations (13) and (15) both can be respectively found as in reference [9] to be:

$$G(\phi) = \frac{\pi |P(\phi)|^2}{2 \sum_{n=-\infty}^{\infty} |A_n|^2} \quad (16)$$

$$G_a/\lambda_0 = \frac{\eta_0 \sum_{n=-\infty}^{\infty} |A_n|^2}{2\pi a^2 \left(\sum_{L=1}^N E_{oL} 2\theta_L \right)^2} \quad (17)$$

where η_0 is the free space intrinsic impedance given by 120π approximately [13, 14].

6. CORRECTNESS OF DERIVATIONS

The series in Equation (12) is from $-\infty$ to $+\infty$ over n and can create infinite matrices in Equation (13). For small values of d this series quickly converges and can be solved by numerical reduction to form finite matrices. On the contrary, for larger values of d the physical size of the proposed structure in Figure 1 is larger and we require further terms in the summation [15]. In view of that, our numerical estimations are only obtained for small eccentricities in order to smooth the progress of the series expansion.

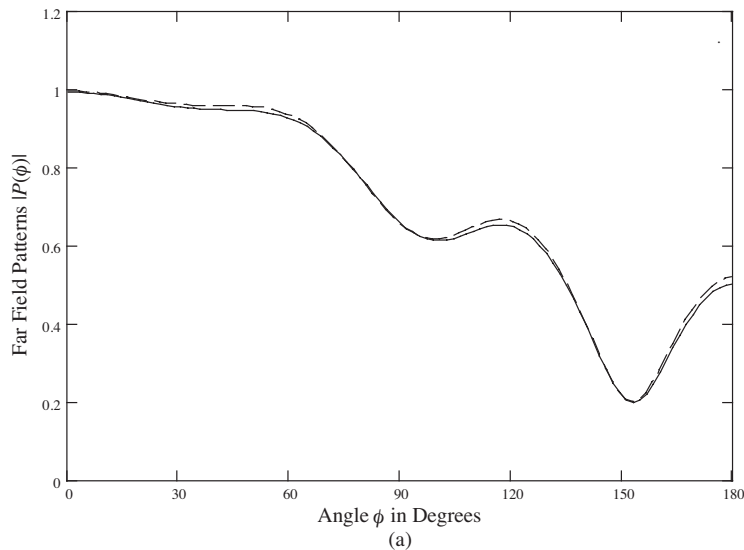
Prior to determining the numerical results for the effects of eccentricity and the slots' arbitrary positions, it is necessary to validate the accuracy of the expressions derived. A number of graphical results are presented and also compared to other curves in references [3, 4, 9] for a slot size of $\theta_0 = \pi/100$. The results found are only calculated for values of n from -25 to 25 of the series formed in the solution due to the rapid convergence of the summation. A smaller number of terms in the summations produced non-satisfactorily results. All produced patterns are normalized to one of the curves as a reference data to simplify our intended investigations and recognize the variations that may happen when N slots of arbitrary position exist with eccentricity.

The radiated patterns in Equation (15) assuming very small eccentricity compared with the results in reference [3] are shown in Figure 2(a) for $N = 1$, $\theta_{s1} = 0$, $2\theta_1 = \theta_0$, $d = 0.001\lambda_0$, $\varepsilon/\varepsilon_0 = 2.56$, $\mu/\mu_0 = 1$, $a = 0.358\lambda_0$ and $b = 0.4217\lambda_0$. Also, in Figure 2(b) the field pattern is compared with related values in reference [4] case II

for $N = 1$, $\theta_{s1} = 0$, $2\theta_1 = \theta_0$, $d = 0.001\lambda_0$, $\varepsilon/\varepsilon_0 = 1$, $\mu/\mu_0 = 4$, $a = 0.318\lambda_0$ and $b = 0.350\lambda_0$. From reference [4], $aA = k_0$ and $bB = k_0$ respectively. In addition, from Equation (16) the antenna gain compared to reference [9] is shown in Figure 3(a) versus the coating thickness at slot location $\phi = 0$ for $N = 1$, $\theta_{s1} = 0$, $2\theta_1 = \theta_0$, $d = 0.001\lambda_0$, $\varepsilon/\varepsilon_0 = 4$, $\mu/\mu_0 = 1$ and $a = 2\lambda_0$. Also, in Figure 3(b) the aperture conductance per unit length λ_0 in Equation (17) is shown versus the coating thickness for $N = 1$, $\theta_{s1} = 0$, $2\theta_1 = \theta_0$, $d = 0.001\lambda_0$, $\varepsilon/\varepsilon_0 = 4$, $\mu/\mu_0 = 1$ and $a = 2\lambda_0$ estimated against the same results in reference [9]. As expected from Figures 2 and 3, the curves demonstrate complete agreements and our results confirm every indication of accuracy. Also, convergence tests illustrate that a sufficient number of terms in the infinite series is applied.

7. EXAMPLES AND DISCUSSIONS

Numerical results in reference [8] are only limited for two slots of a fixed size located at $\phi = 0$ and π , however, in this study field characteristics are found for N axial slots of arbitrary sizes and positions with an eccentric coating. In this case, sizes and positions of axial slots are two additional variables that can affect the radiation characteristics of the proposed structure such as directivity that may be employed in certain applications. For many possible applications, these two additional variables can greatly help in some design and construction situations in addition to other parameters.



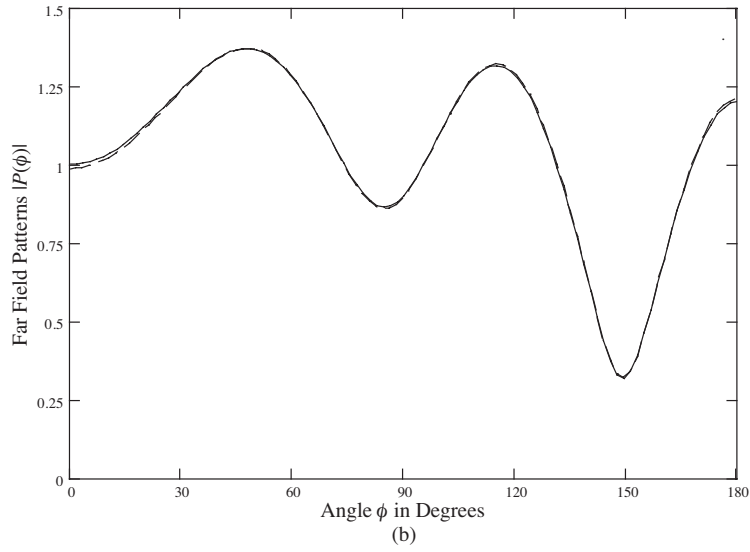
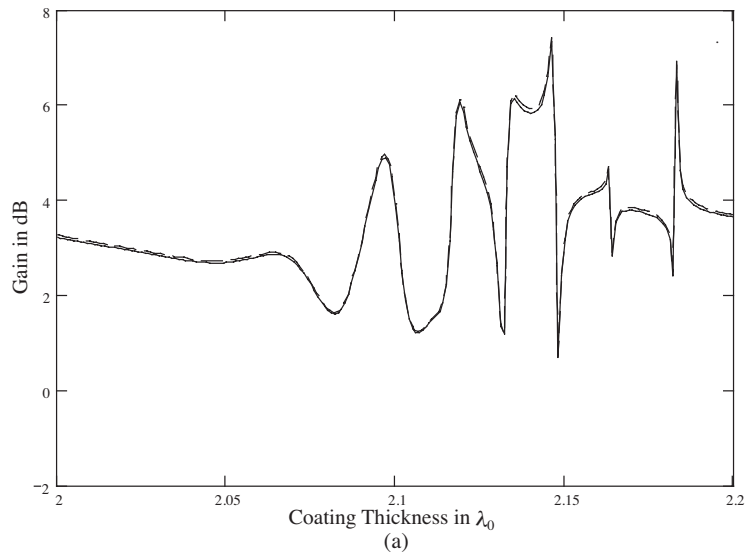


Figure 2. (a) Radiation patterns for $\varepsilon/\varepsilon_0 = 2.56$, $\mu/\mu_0 = 1$, $a = 0.358\lambda_0$ and $b = 0.4217\lambda_0$. — reference [3], - - - - calculated for $N = 1$, $\theta_{s1} = 0$, $2\theta_1 = \theta_0$, and $d = 0.001\lambda_0$. (b) Radiation patterns for $\varepsilon/\varepsilon_0 = 1$, $\mu/\mu_0 = 4$, $a = 0.318\lambda_0$ and $b = 0.350\lambda_0$. — reference [4], - - - - calculated for $N = 1$, $\theta_{s1} = 0$, $2\theta_1 = \theta_0$, and $d = 0.001\lambda_0$.



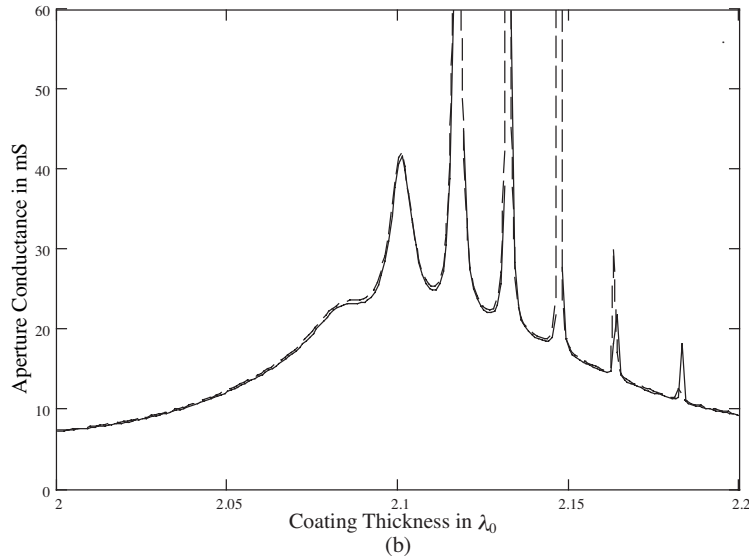


Figure 3. (a) Antenna gain versus coating thickness for $\varepsilon/\varepsilon_0 = 4$, $\mu/\mu_0 = 1$ and $a = 2\lambda_0$. — reference [9], - - - - calculated at $\phi = 0$ for $N = 1$, $\theta_{s1} = 0$, $2\theta_1 = \theta_0$, and $d = 0.001\lambda_0$. (b) Aperture conductance versus coating thickness for $\varepsilon/\varepsilon_0 = 4$, $\mu/\mu_0 = 1$ and $a = 2\lambda_0$ — reference [9], - - - - calculated for $N = 1$, $\theta_{s1} = 0$, $2\theta_1 = \theta_0$, and $d = 0.001\lambda_0$.

The radiated far field patterns are better be viewed and examined in polar coordinates. Parameters such as a , b , $\varepsilon/\varepsilon_0$ and μ/μ_0 are selected as in references [3,4,9] for all obtained numerical results for comparison purposes. Also, numerical results of the radiation characteristics are calculated for $N = 1, 2$ and 3 only.

Figure 4(a) illustrates the radiation patterns for $N = 1$, $2\theta_1 = \theta_0$, $a = 0.358\lambda_0$, $b = 0.4217\lambda_0$, $\varepsilon/\varepsilon_0 = 2.56$, $\mu/\mu_0 = 1$ and $d = 0\lambda_0$, $0.02\lambda_0$ and $0.06\lambda_0$ respectively. The main lobe at $\phi = 0$ decreases as d increases which indicate a lower radiation of energy at this direction with respect to eccentricity. Figure 4(b) also shows the radiation patterns for $N = 1$, $2\theta_1 = \theta_0$, $a = 0.358\lambda_0$, $b = 0.4217\lambda_0$, $\varepsilon/\varepsilon_0 = 1$, $\mu/\mu_0 = 4$ and $d = 0\lambda_0$, $0.02\lambda_0$ and $0.06\lambda_0$ respectively. Also, the patterns generally decrease as d increases, however, the main radiation lobe at $\phi = 0$ broadens as d increases.

Figure 5(a) shows the radiation patterns for $N = 2$, $\theta_{s1} = 0$, $\theta_{s2} = \pi$, $2\theta_1 = 2\theta_2 = \theta_0$, $a = 0.358\lambda_0$, $b = 0.4217\lambda_0$, $\varepsilon/\varepsilon_0 = 2.56$, $\mu/\mu_0 = 1$ and $d = 0\lambda_0$, $0.02\lambda_0$ and $0.06\lambda_0$ respectively. Although d

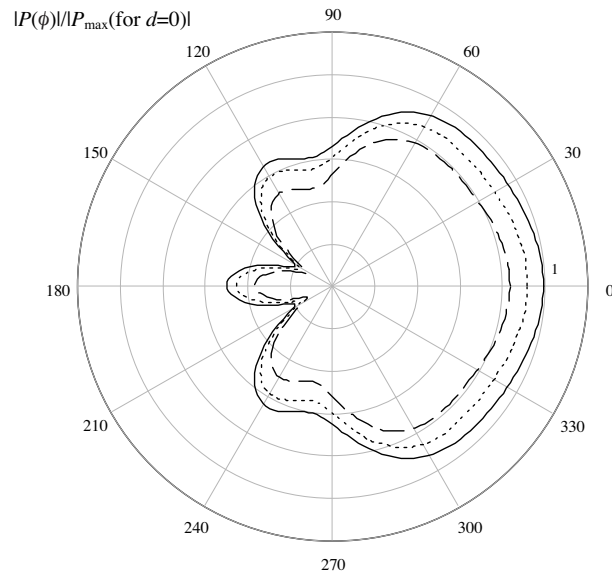
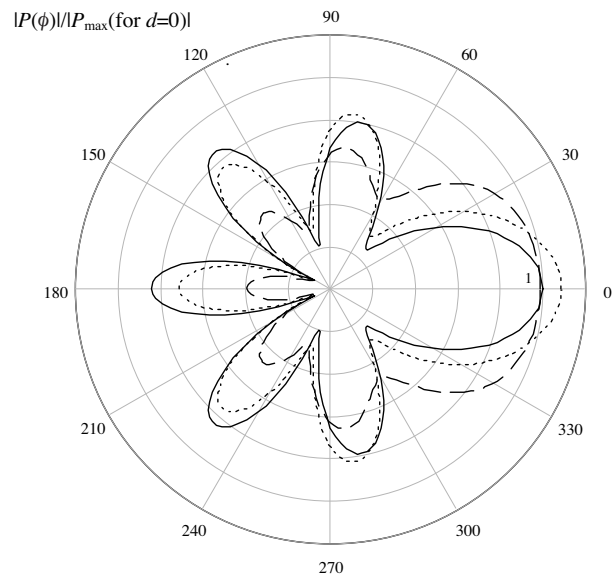
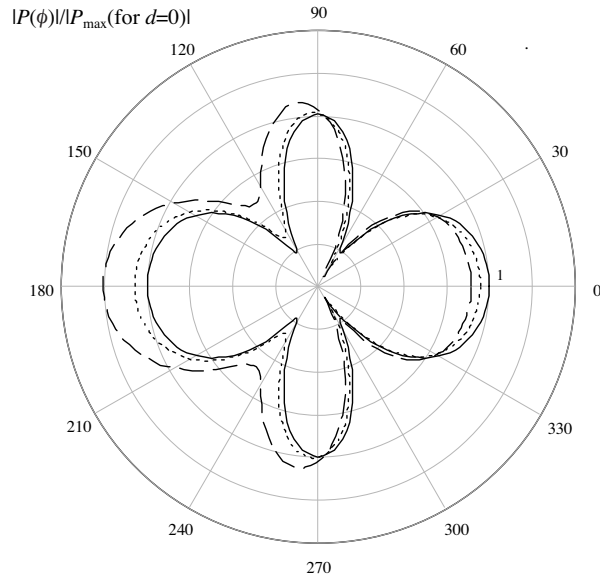
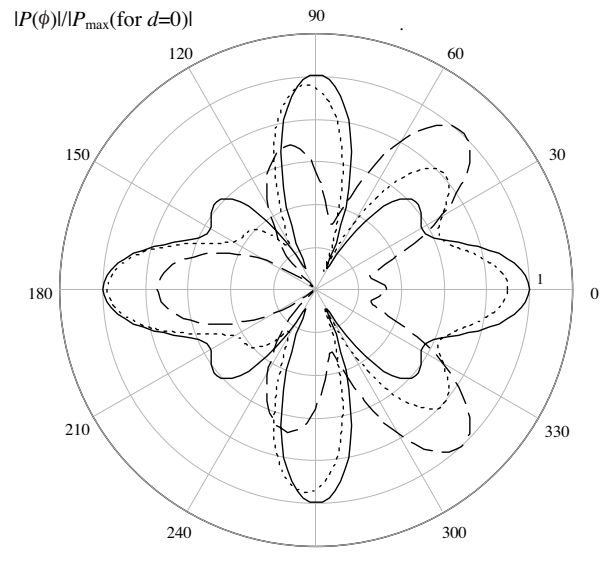
(a) $\varepsilon/\varepsilon_0=2.56, \mu/\mu_0=1$ (b) $\varepsilon/\varepsilon_0=1, \mu/\mu_0=4$

Figure 4. Radiation patterns for $N = 1$, $\theta_{s1} = 0$, $2\theta_1 = \theta_0$, $a = 0.358\lambda_0$ and $b = 0.4217\lambda_0$. — $d = 0\lambda_0$, $\cdots\cdots d = 0.02\lambda_0$, $----- d = 0.06\lambda_0$.



(a) $\epsilon/\epsilon_0=2.56, \mu/\mu_0=1$



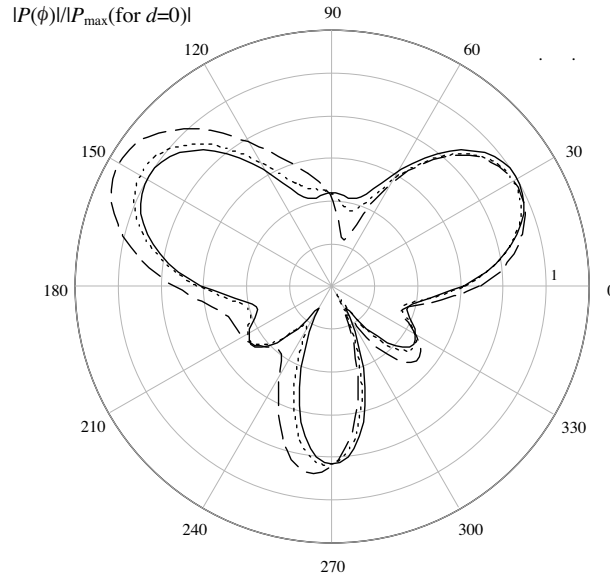
(b) $\epsilon/\epsilon_0=1, \mu/\mu_0=4$

Figure 5. Radiation patterns for $N = 2, \theta_{s1} = 0, \theta_{s2} = \pi, 2\theta_1 = 2\theta_2 = \theta_0, a = 0.358\lambda_0$ and $b = 0.4217\lambda_0$. — $d = 0\lambda_0, \dots\dots d = 0.02\lambda_0, - - - - d = 0.06\lambda_0$.

increases we can notice an increase of the field at $\phi = \pi$ and a decrease at $\phi = 0$. Figure 5(b) also shows the radiation patterns for $N = 2$, $\theta_{s1} = 0$, $\theta_{s2} = \pi$, $2\theta_1 = 2\theta_2 = \theta_0$, $a = 0.358\lambda_0$, $b = 0.4217\lambda_0$, $\varepsilon/\varepsilon_0 = 1$, $\mu/\mu_0 = 4$, and $d = 0\lambda_0$, $0.02\lambda_0$ and $0.06\lambda_0$ respectively. In this case the patterns are changed particularly at $\phi = 0$ where the field is decreased for $d = 0.06\lambda_0$.

In Figure 6(a), the radiation patterns are plotted for $N = 3$, $\theta_{s1} = 0$, $\theta_{s2} = \pi/2$, $\theta_{s3} = \pi$, $2\theta_1 = 2\theta_2 = 2\theta_3 = \theta_0$, $a = 0.358\lambda_0$, $b = 0.4217\lambda_0$, $\varepsilon/\varepsilon_0 = 2.56$, $\mu/\mu_0 = 1$ and $d = 0\lambda_0$, $0.02\lambda_0$ and $0.06\lambda_0$ respectively. As d increases we can notice an increase of the field at different angles. Also, Figure 6(b) also shows the radiation patterns for $N = 3$, $\theta_{s1} = 0$, $\theta_{s2} = \pi/2$, $\theta_{s3} = \pi$, $2\theta_1 = 2\theta_2 = 2\theta_3 = \theta_0$, $a = 0.358\lambda_0$, $b = 0.4217\lambda_0$, $\varepsilon/\varepsilon_0 = 1$, $\mu/\mu_0 = 4$ and $d = 0\lambda_0$, $0.02\lambda_0$ and $0.06\lambda_0$ respectively. Here, the fields are highly varied with additional lobes and a clear increase for $d = 0.06\lambda_0$ at $\phi \approx 50$ degrees.

Figure 7 illustrates the radiated fields as the slot location is changed with eccentricity for $N = 1$, $2\theta_1 = \theta_0$, $a = 0.358\lambda_0$, $b = 0.4217\lambda_0$, $d = 0.06\lambda_0$ and $\theta_{s1} = \pi/4$, $\pi/2$ and $3\pi/4$ respectively. In Figure 7(a), fields are found for $\varepsilon/\varepsilon_0 = 2.56$ and $\mu/\mu_0 = 1$ where the radiations are highest for $\theta_{s1} = 3\pi/4$ but with a different main lobe angle of about 135 degrees. Greater variations and distortions are shown in Figure 7(b) for $\varepsilon/\varepsilon_0 = 1$ and $\mu/\mu_0 = 4$.



(a) $\varepsilon/\varepsilon_0=2.56$, $\mu/\mu_0=1$

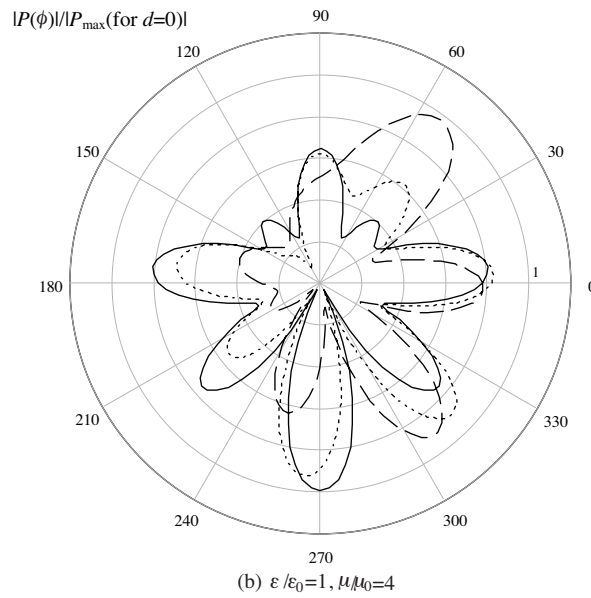
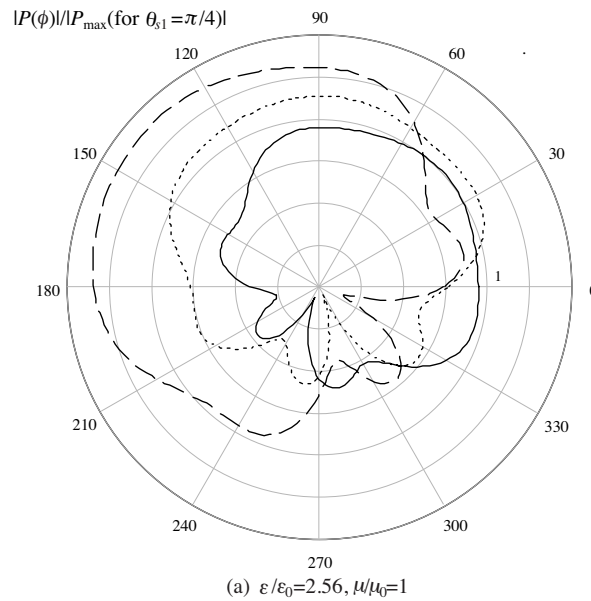


Figure 6. Radiation patterns for $N = 3$, $\theta_{s1} = 0$, $\theta_{s2} = \pi/2$, $\theta_{s3} = \pi$, $2\theta_1 = 2\theta_2 = 2\theta_3 = \theta_0$, $a = 0.358\lambda_0$ and $b = 0.4217\lambda_0$, — $d = 0\lambda_0$, $d = 0.02\lambda_0$, - - - - $d = 0.06\lambda_0$.



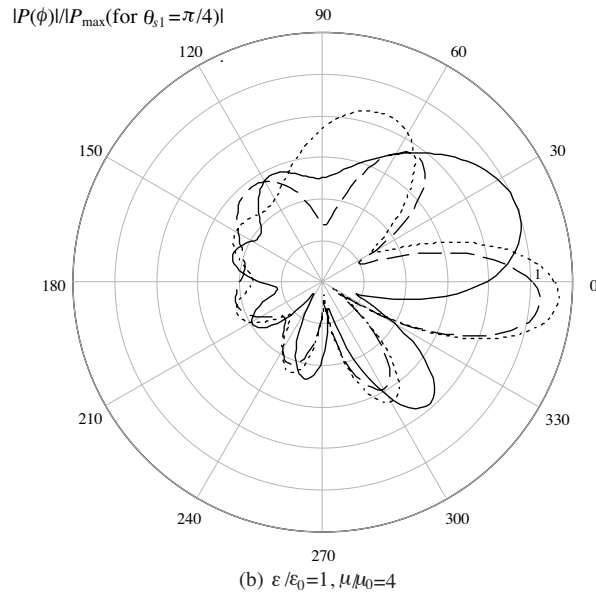
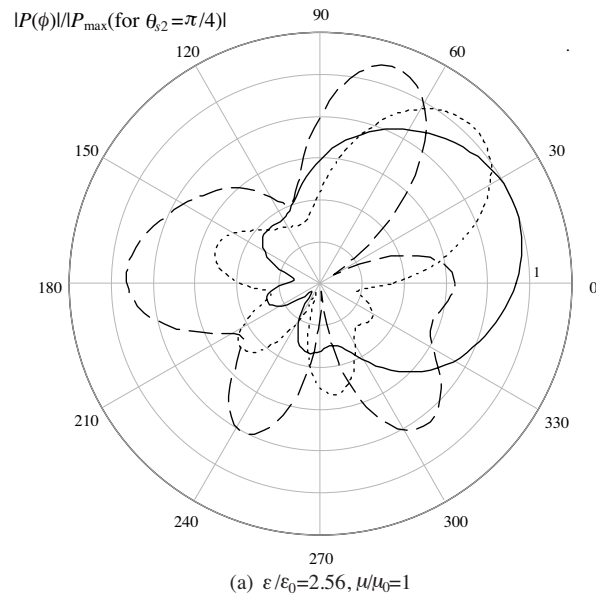


Figure 7. Radiation patterns for $N = 1$, $2\theta_1 = \theta_0$, $a = 0.358\lambda_0$, $b = 0.4217\lambda_0$ and $d = 0.06\lambda_0$. — $\theta_{s1} = \pi/4$, $\cdots\cdots\theta_{s1} = \pi/2$, $-----\theta_{s1} = 3\pi/4$.



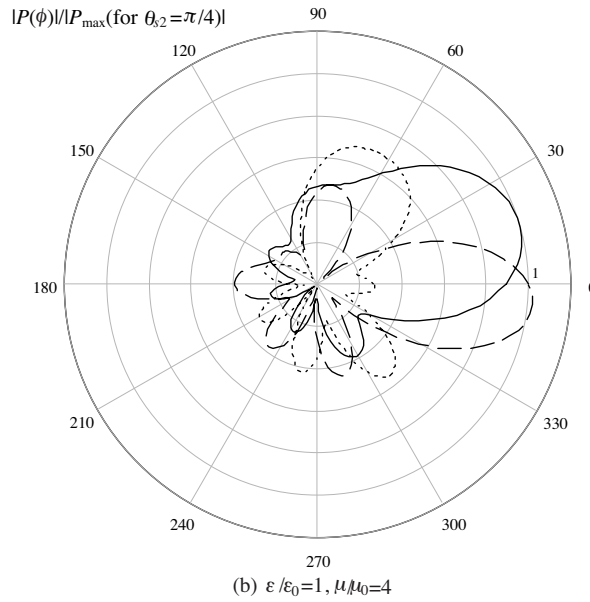
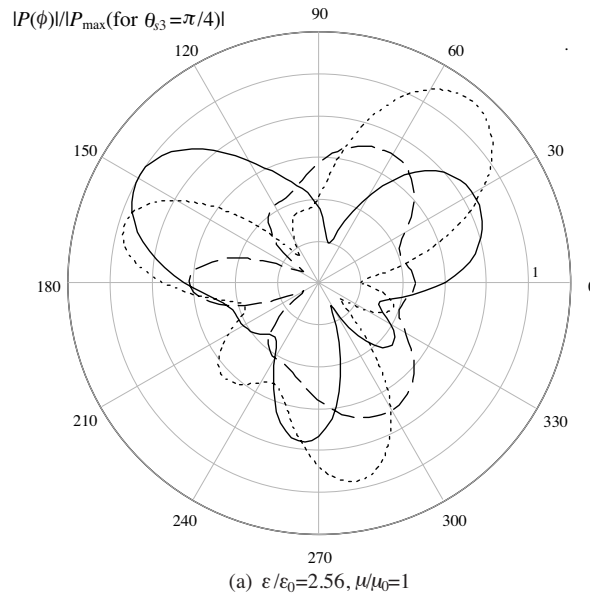


Figure 8. Radiation patterns for $N = 2$, $\theta_{s1} = 0$, $2\theta_1 = 2\theta_2 = \theta_0$, $a = 0.358\lambda_0$, $b = 0.4217\lambda_0$ and $d = 0.06\lambda_0$, — $\theta_{s2} = \pi/4$, $\theta_{s2} = \pi/2$, - - - $\theta_{s2} = 3\pi/4$.



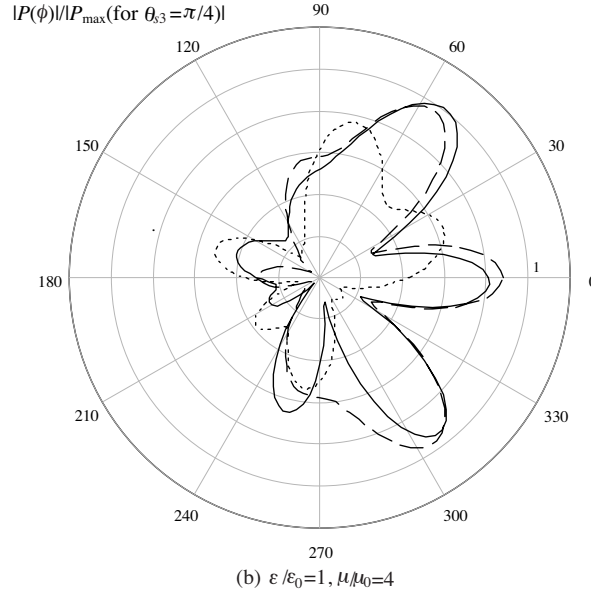


Figure 9. Radiation patterns for $N = 3$, $\theta_{s1} = 0$, $\theta_{s2} = \pi/2$, $2\theta_1 = 2\theta_2 = 2\theta_3 = \theta_0$, $a = 0.358\lambda_0$, $b = 0.4217\lambda_0$ and $d = 0.06\lambda_0$, — $\theta_{s3} = \pi$, $\cdots\cdots\theta_{s3} = 5\pi/4$, - - - $\theta_{s3} = 3\pi/2$.

In addition, Figure 8 shows the radiated fields as the second slot location is changed with eccentricity for $N = 2$, $\theta_{s1} = 0$, $2\theta_1 = 2\theta_2 = \theta_0$, $a = 0.358\lambda_0$, $b = 0.4217\lambda_0$, $d = 0.06\lambda_0$ and $\theta_{s2} = \pi/4$, $\pi/2$ and $3\pi/4$ respectively. In Figure 8(a), fields are plotted for $\varepsilon/\varepsilon_0 = 2.56$ and $\mu/\mu_0 = 1$ where the radiations are generally highest for $\theta_{s1} = 3\pi/4$ but with more lobes and deformations. Larger changes are shown in Figure 8(b) for $\varepsilon/\varepsilon_0 = 1$ and $\mu/\mu_0 = 4$.

Furthermore, Figure 9 illustrates the patterns as the third slot location is changed with eccentricity for $N = 3$, $\theta_{s1} = 0$, $\theta_{s2} = \pi/2$, $2\theta_1 = 2\theta_2 = 2\theta_3 = \theta_0$, $a = 0.358\lambda_0$, $b = 0.4217\lambda_0$, $d = 0.06\lambda_0$ and $\theta_{s3} = \pi$, $5\pi/4$ and $3\pi/2$ respectively. In Figure 9(a), radiations are calculated for $\varepsilon/\varepsilon_0 = 2.56$ and $\mu/\mu_0 = 1$ where the radiations are varied with many lobes at different angles. Other changes are also shown in Figure 9(b) for $\varepsilon/\varepsilon_0 = 1$ and $\mu/\mu_0 = 4$.

The antenna gain in dB versus coating thickness at $\phi = 0$ is plotted in Figure 10 for $N = 1$, $\theta_{s1} = 0$, $2\theta_1 = \theta_0$, $a = 2\lambda_0$, and $d = 0\lambda_0$, $0.02\lambda_0$ and $= 0.06\lambda_0$ respectively. In Figure 10(a), the gain peaks are changed with respect to the coating thickness as eccentricity changes for $\varepsilon/\varepsilon_0 = 4$ and $\mu/\mu_0 = 1$. Also, in Figure 10(b) the gain is varied

with respect to the coating thickness for $\epsilon/\epsilon_0 = 1$ and $\mu/\mu_0 = 4$ as eccentricity increases.

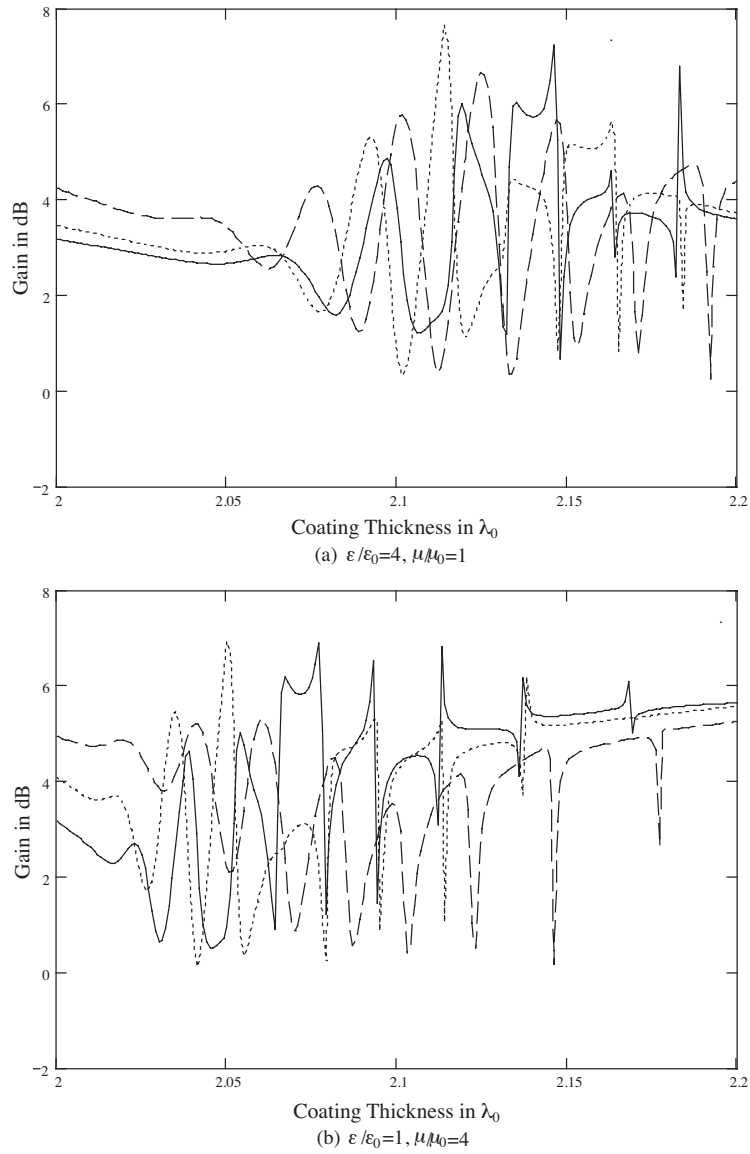


Figure 10. Antenna gain versus coating thickness at $\phi = 0$ for $N = 1$, $\theta_{s1} = 0$, $2\theta_1 = \theta_0$ and $a = 2\lambda_0$. — $d = 0\lambda_0$, $\cdots\cdots$ $d = 0.02\lambda_0$, - - - $d = 0.06\lambda_0$.

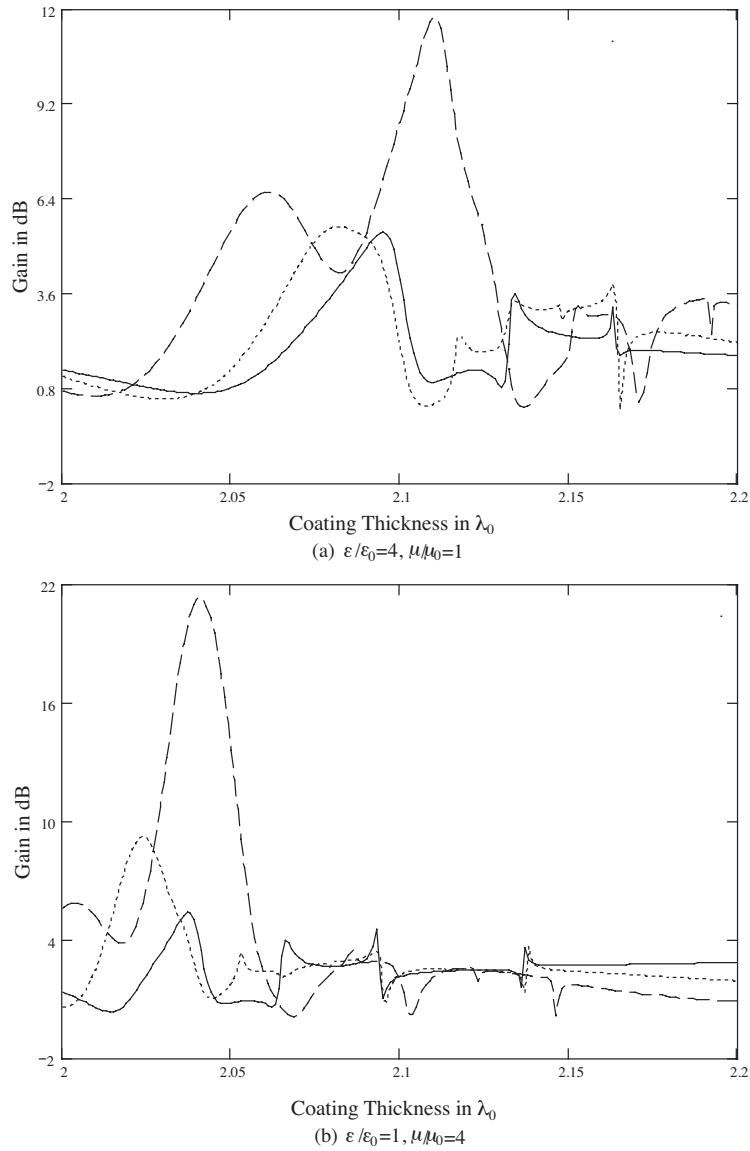


Figure 11. Antenna gain versus coating thickness at $\phi = 0$ for $N = 2$, $\theta_{s1} = 0$, $\theta_{s2} = \pi$, $2\theta_1 = 2\theta_2 = \theta_0$ and $a = 2\lambda_0$. — $d = 0\lambda_0$, $\cdots\cdots$ $d = 0.02\lambda_0$, $-----$ $d = 0.06\lambda_0$.

Great changes in the gain at $\phi = 0$ are shown in Figure 11 for $N = 2$, $\theta_{s1} = 0$, $\theta_{s2} = \pi$, $2\theta_1 = 2\theta_2 = \theta_0$, $a = 2\lambda_0$, and $d = 0\lambda_0$,

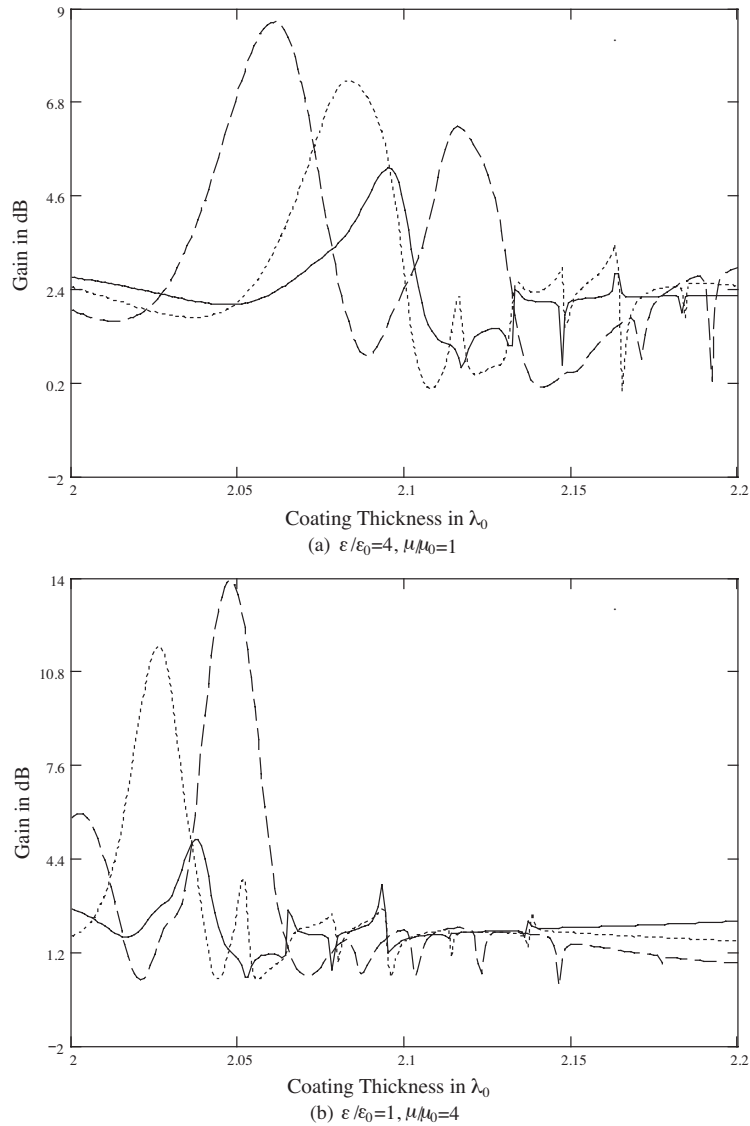


Figure 12. Antenna gain versus coating thickness at $\phi = 0$ for $N = 3$, $\theta_{s1} = 0$, $\theta_{s2} = \pi/2$, $\theta_{s3} = \pi$, $2\theta_1 = 2\theta_2 = 2\theta_3 = \theta_0$ and $a = 2\lambda_0$, — $d = 0\lambda_0$, $\cdots \cdots d = 0.02\lambda_0$, - - - - $d = 0.06\lambda_0$.

$0.02\lambda_0$ and $= 0.06\lambda_0$ respectively. In Figure 11(a), the uppermost peak for $\epsilon/\epsilon_0 = 4$ and $\mu/\mu_0 = 1$ is shown for $d = 0.06\lambda_0$ at $b \approx 2.11\lambda_0$

approximately. However, in Figure 11(b) the primary peak for $\varepsilon/\varepsilon_0 = 1$ and $\mu/\mu_0 = 4$ is also shown for $d = 0.06\lambda_0$ but at $b \approx 2.04\lambda_0$ approximately.

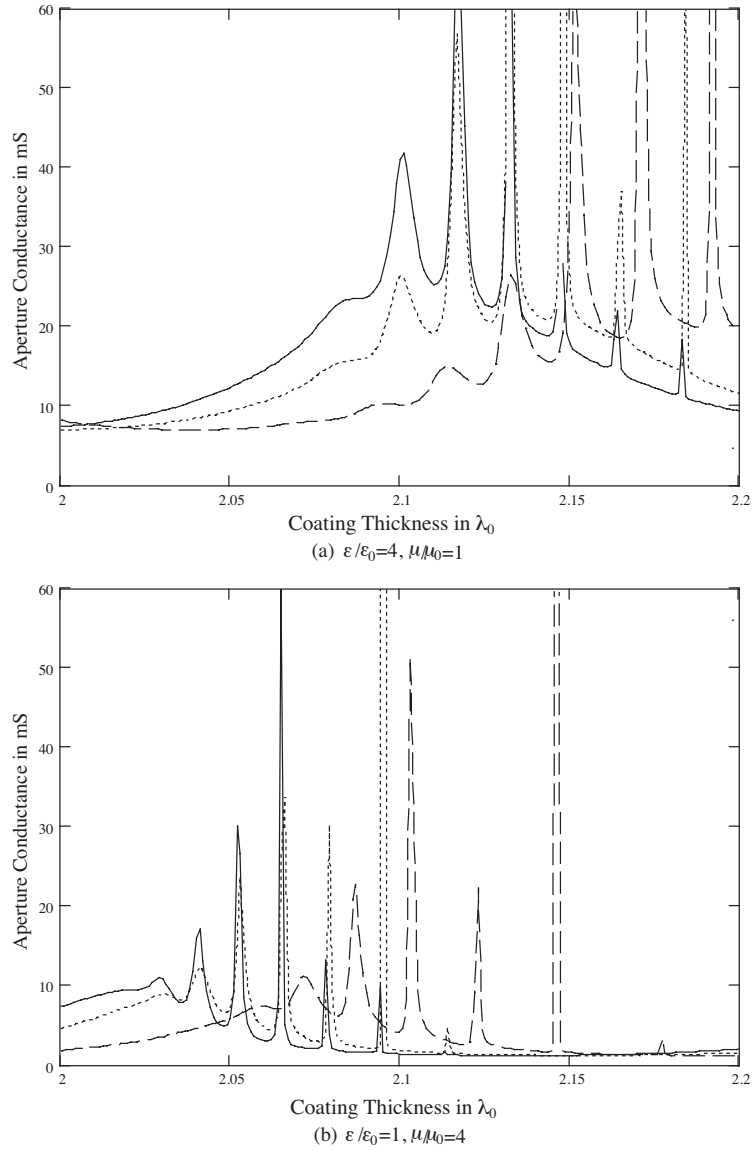
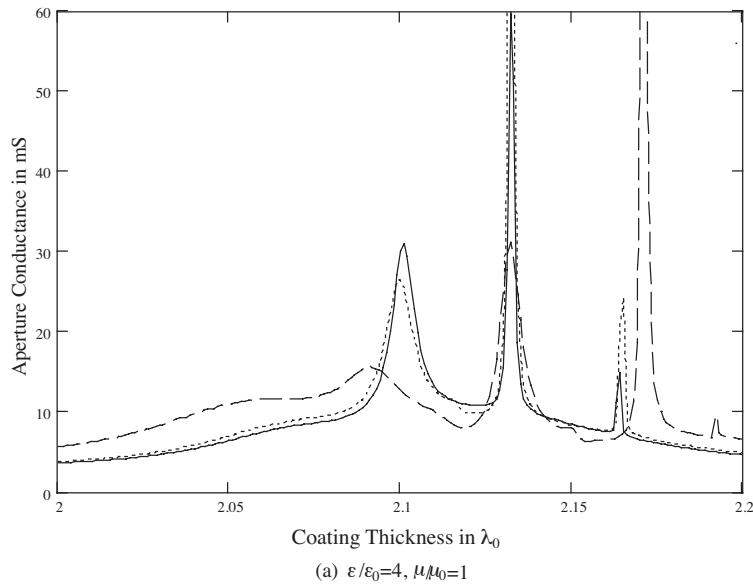


Figure 13. Aperture Conductance versus coating thickness for $N = 1$, $\theta_{s1} = 0$, $2\theta_1 = \theta_0$, $a = 2\lambda_0$. — $d = 0\lambda_0$, $\cdots\cdots d = 0.02\lambda_0$, - - - $d = 0.04\lambda_0$, - · - · $d = 0.06\lambda_0$.

In addition, Figure 12 shows the gain versus the coating thickness at $\phi = 0$ for $N = 3$, $\theta_{s1} = 0$, $\theta_{s2} = \pi/2$, $\theta_{s3} = \pi$, $2\theta_1 = 2\theta_2 = 2\theta_3 = \theta_0$ and $d = 0\lambda_0$, $0.02\lambda_0$ and $= 0.06\lambda_0$ respectively. For $\varepsilon/\varepsilon_0 = 4$ and $\mu/\mu_0 = 1$, the gain is plotted in Figure 12(a) where the highest peak is found for $d = 0.06\lambda_0$ at $b \approx 2.06\lambda_0$ approximately. In Figure 12(b) for $\varepsilon/\varepsilon_0 = 1$ and $\mu/\mu_0 = 4$, the main peak is located around $b \approx 2.05\lambda_0$ for $d = 0.06\lambda_0$.

The aperture conductance in mille siemens (mS) versus coating thickness is shown in Figure 13 for $N = 1$, $\theta_{s1} = 0$, $2\theta_1 = \theta_0$, $a = 2\lambda_0$ and $d = 0\lambda_0$, $0.02\lambda_0$ and $= 0.06\lambda_0$ respectively. In Figure 13(a), this quantity decreases as d increases for the values shown for $\varepsilon/\varepsilon_0 = 4$ and $\mu/\mu_0 = 1$. Figure 13(b) illustrates the changes for $\varepsilon/\varepsilon_0 = 1$ and $\mu/\mu_0 = 4$. Resonant points with respect to the coating thickness may greatly affect the radiation patterns and enhance the radiated power. In this figure, these points are almost the same for $d = 0\lambda_0$ and $0.02\lambda_0$ but there are slight shifts for $d = 0.06\lambda_0$.

Moreover, Figure 14 shows the aperture conductance versus coating thickness for $N = 2$, $\theta_{s1} = 0$, $\theta_{s2} = \pi$, $2\theta_1 = 2\theta_2 = \theta_0$ and $d = 0\lambda_0$, $0.02\lambda_0$ and $= 0.06\lambda_0$ respectively. Many variations are shown in Figure 14(a) for $\varepsilon/\varepsilon_0 = 4$ and $\mu/\mu_0 = 1$. In Figure 14(b), this quantity is generally minimized for $\varepsilon/\varepsilon_0 = 1$ and $\mu/\mu_0 = 4$. Resonances are about equivalent for $d = 0\lambda_0$ and $0.02\lambda_0$ but with minor changes for $d = 0.06\lambda_0$.



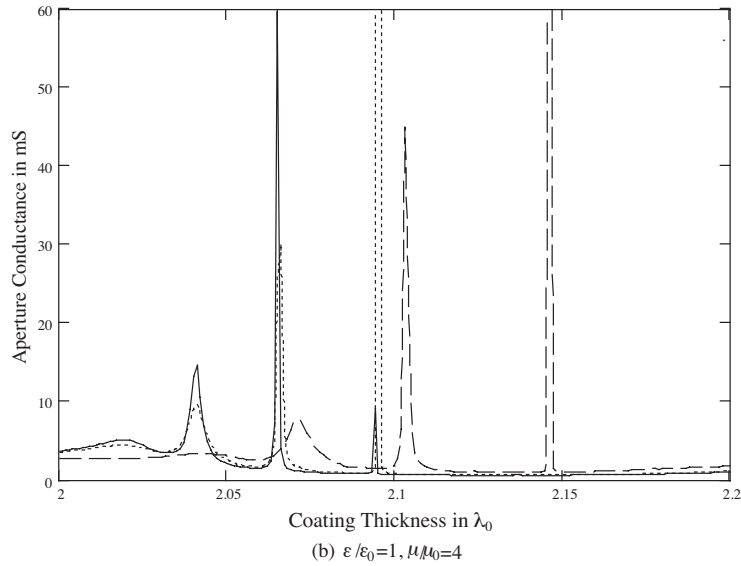
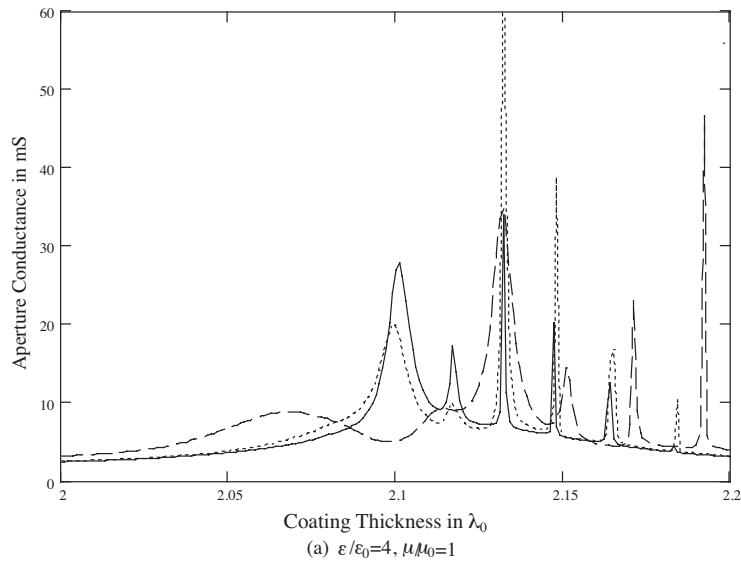


Figure 14. Aperture Conductance versus coating thickness for $N = 2$, $\theta_{s1} = 0$, $\theta_{s2} = \pi$, $2\theta_1 = 2\theta_2 = \theta_0$ and $a = 2\lambda_0$, — $d = 0\lambda_0$, $d = 0.02\lambda_0$, - - - - $d = 0.06\lambda_0$.

Finally, Figure 15 shows the aperture conductance versus coating thickness for $N = 3$, $\theta_{s1} = 0$, $\theta_{s2} = \pi/2$, $\theta_{s3} = \pi$, $2\theta_1 = 2\theta_2 = 2\theta_3 = \theta_0$



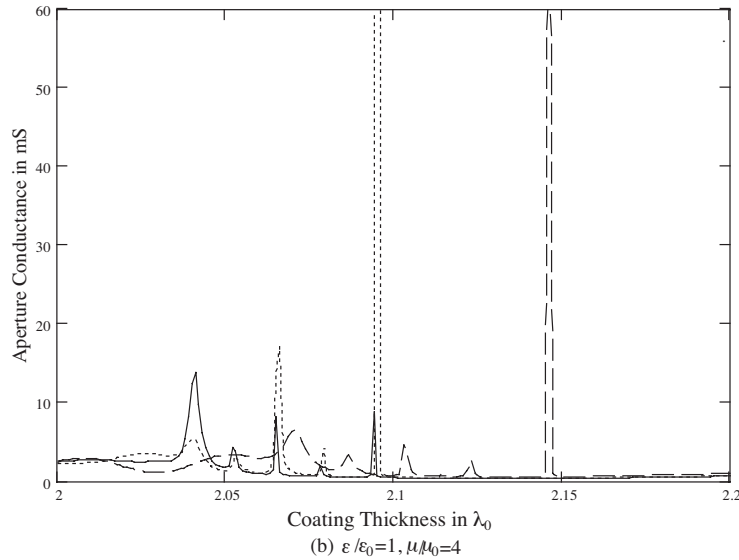


Figure 15. Aperture Conductance versus coating thickness for $N = 3$, $\theta_{s1} = 0$, $\theta_{s2} = \pi/2$, $\theta_{s3} = \pi$, $2\theta_1 = 2\theta_2 = 2\theta_3 = \theta_0$ and $a = 2\lambda_0$, — $d = 0\lambda_0$, $\cdots\cdots d = 0.02\lambda_0$, — — — $d = 0.06\lambda_0$.

and $d = 0\lambda_0$, $0.02\lambda_0$ and $= 0.06\lambda_0$ respectively. More peaks appeared in Figure 15(a) for $\varepsilon/\varepsilon_0 = 4$ and $\mu/\mu_0 = 1$. The aperture conductance is also minor for $\varepsilon/\varepsilon_0 = 1$ and $\mu/\mu_0 = 4$ as shown in Figure 15(b). Also, resonances are changed for $d = 0.06\lambda_0$ but approximately equal for $d = 0\lambda_0$ and $0.02\lambda_0$.

8. CONCLUSION

A solution was derived for the problem of N infinite axial slots of arbitrary sizes and positions in a circular cylinder covered with an eccentric coating material. The TE case was considered based on the boundary value method and the radiated fields were represented in terms of an infinite series of cylindrical waves. The solution explained the effects of the proposed additional slots with eccentricity to the far field patterns in addition to the influences that can arise to the antenna gain and the aperture conductance.

REFERENCES

1. Silver, S. and W. Saunders, "The external field produced by a slot in an infinite circular cylinder," *Journal of Applied Physics*,

- Vol. 21, No. 5, 153–158, February 1950.
2. Bailin, L. L., “The radiation field produced by a slot in a large circular cylinder,” *IRE Transactions — Antennas and Propagation*, Vol. 3, No. 3, 128–137, July 1955.
 3. Hurd, R. A., “Radiation patterns of a dielectric-coated axially slotted cylinder,” *Canadian Journal of Physics*, Vol. 34, 638–642, 1956.
 4. Wait, J. and W. Mientka, “Slotted-cylinder antenna with a dielectric coating,” *Journal of Research of the National Bureau of Standards*, Vol. 58, No. 6, 287–296, June 1957.
 5. Jordan, E. O. and W. E. Miller, “Slotted-cylinder antenna,” *Electronics*, 90–93, February 1947.
 6. Leung, K. W. and L. Y. Chan, “The probe-fed zonal slot antenna cut onto a cylindrical conducting cavity,” *IEEE Transactions on Antennas and Propagation*, Vol. 53, No. 12, 3949–3952, December 2005.
 7. Mushref, M. A., “Radiation from a dielectric-coated cylinder with two slots,” *Applied Mathematics Letters*, Vol. 17, No. 6, 721–726, June 2004.
 8. Mushref, M. A., “Field characteristics from an eccentric dielectric coated circular cylinder with two axial slots,” *Electromagnetics*, Vol. 25, No. 1, 55–67, January 2005.
 9. Richmond, J., “Axial slot antenna on a dielectric-coated elliptic cylinder,” *IEEE Transactions on Antennas and Propagation*, Vol. 37, No. 10, 1235–1241, October 1989.
 10. Chew, W. C., *Waves and Fields in Inhomogeneous Media*, IEEE, New York, 1995.
 11. Harrington, R. F., *Time-harmonic Electromagnetic Fields*, IEEE, New York, 2001.
 12. Stratton, J. A., *Electromagnetic Theory*, McGraw-Hill Book Company, Inc., New York, 1941.
 13. Morse, P. M. and H. Feshbach, *Methods of Theoretical Physics*, parts I and II, McGraw-Hill Book Company, Inc., New York, 1953.
 14. Knop, C. M., “External admittance of an axial slot on a dielectric coated metal cylinder,” *Radio Science*, Vol. 3 (new series), No. 8, 803–817, August 1968.
 15. Mushref, M. A., “Matrix solution to electromagnetic scattering by a conducting cylinder with an eccentric metamaterial coating,” *Journal of Mathematical Analysis and Applications*, Vol. 332, No. 1, 356–366, August 2007.